PAPER

Check for updates

Mussel-inspired *in situ* fabrication of a photothermal composite hydrogel for MR-guided localized tumor ablation

Lixia Xu,†[ab] Ronghua Qin,†[b] Jingjing Zhang,[b] Jinjin Liu,[b] Suwan Liu,[b] Feng Li,[b] Aihua Gong,[b] Qian Hanliang,*[a] Fengyi Du [ID] *[b] and Miaomiao Zhang*[b]

Photothermal ablation could be considered an effective treatment for tumors, but accurate administration and enrichment of photothermal agents remain a huge challenge. Herein, a mussel-inspired photothermal polymeric hydrogel (PPH) was synthesized through a ferric iron-triggered simultaneous metal–catechol coordination reaction and oxidative polymerization of covalently linked pyrrole. The PPH with rapid gelation (less than 10 s) exhibited high photothermal conversion efficiency (49.3%), which enabled effective hyperthermal therapy *in situ*. Besides, the introduced iron could be used as a T_2-weighted contrast agent for real-time MR imaging to explore the retention and bio-degradation of PPH *in vivo*. Overall, our findings evidence that the resultant PPH, which possesses potential application in tumor ablation *in situ*, and metal–catechol coordination strategy inspired by mussel adhesion may stimulate biomedical hydrogel development.

1 Introduction

Photothermal therapy (PTT) is a promising treatment technology using hyperthermia to eradicate solid tumors.[1] During the process, certain photosensitizers (PS) concentrated in the tumor area generate heat to increase the local temperature of tumor tissues under laser irradiation.[2] At 40–45 °C, the biomacromolecules in tumor cells, such as proteins, nucleic acids and lipids, will suffer irreversible damage, thereby the tumors are destroyed.[3] Furthermore, due to the disordered vascular network and blocked blood vessels caused by PTT, tumor cells are more sensitive than normal tissues. Due to the obvious advantages, PTT-based technology is increasingly being developed and used in cancer treatment and research. Many inorganic materials (gold nanostructures,[4,5] palladium nanoflakes and metal sulfide nanoparticles) and organic materials (carbon-based nanoscale materials, near-infrared (NIR) dyes, polydopamine (PDA),[6,7] and polypyrrole (PPY)) have been explored as PS for effective PTT applications.[8,9] Among them, PPY has attracted great interest and attention due to its inherent excellent near infrared photothermal conversion ability, photothermal stability and good bio-compatibility.[10–12] Polypyrrole (PPY) can be formed by pyrrole through coordination polymerization in the presence of an oxidant (such as Fe^{3+}) by an electro chemical

coupling reaction.[13,14] It is worth noting that the therapeutic effect of PTT depends heavily on the concentration of PS based on physical method. Despite the EPR effect and targeting modification,[15] it is difficult to achieve an ideal concentration in tumor sites using traditional intravenous administration of PS.[16] Consequently, it is urgent to develop novel PS delivery system to achieve the desired PTT therapeutic effect.

Injectable hydrogels with good biocompatibility and biodegradability have great prospect in drug delivery *in situ* due to their unique hydrodynamic performance.[17–21] Numerous multifunctional injectable hydrogels were designed and prepared based on distinct principles, such as ion exchange,[22] enzyme catalysis,[23] borate reaction,[24] Schiff Base reaction,[25] Michael addition reaction[26] and catechol-based reaction.[27] It was worth noting that catechol-based hydrogel exhibited favorable advantages in gelation *in situ* as injectable carriers for drug delivery,[28] which ascribed to hydrogen bond formation and metal–catechol coordination interaction.[29,30] The mechanism of catechol-based gelation was derived from adhesion of mussels to turbulent rock surfaces due to their secretion of a protein rich in catechol groups.[31–33] Due to the diversity of catechol chemical properties, a variety of bio-adhesive hydrogel were fabricated *via* polyphenol interaction for wearable devices, biological glue and gelation *in situ*,[34] such as tannin-mediated hydrogel,[35] dopamine-modified hydrogel.[36]

Inspired by those results, we intend to develop a new type of injectable photothermal polymeric hydrogel (PPH) for tumor ablation *in situ*. Firstly, catechol grafted PEI (Cate-PEI) was synthesized using 3,4-dihydroxy hydrocinnamic acid (caffeic acid) as precursor under amide reaction. Then, the PPH was

[a]Department of Ophthalmology, Affiliated Hospital of Jiangsu University, Zhenjiang 212002, Jiangsu, P. R. China

[b]School of Medicine, Jiangsu University, Zhenjiang, 212013, People' s Republic of China. E-mail: biodfy@ujs.edu.cn

† These authors contributed equally to this work.

quickly formed *via* ferric ion-mediated coordination reaction and oxidative polymerization. During the process, ferric ion both used as oxidant for catalyzing pyrrole to form polypyrrole (PPY) and chelating catechol groups in side chain of Cate-PEI. The photothermal conversion efficiency of PPH was calculated and its photothermal therapeutic effect was verified *in vitro* and vivo. In addition, iron element could be used as MRI contrast agent for real-time imaging to guide precise tumor ablation *in vivo*.[37]

2 Experimental

2.1 Chemicals and reagents

All chemicals are used directly without purification and analysis. 3,4-Dihydroxyhydrocinnamic acid (caffeic acid), *N*-(3-dimethylaminopropyl)-*N*′-ethylcarbodiimide hydrochloride (EDC) (≥98.5%), pyrrole (≥99%), iron chloride hexahydrate all were purchased from Aladdin Reagent Co. Ltd. (Shanghai, China). Poly(ethyleneimine) solution (PEI, average $M_w \sim 25$ kDa by LS, 50 wt% in H_2O) was obtained from Sigma-Aldrich (USA).

2.2 Synthesis of Cate-PEI

Cate-PEI was synthesized *via* grafting caffeic acid on the side chain of PEI through EDC chemical reaction. Briefly, 3,4-dihydroxyhydro-cinnamic acid (0.05, 0.125, 0.25, 0.5, 0.75, 1.0, 1.25 mmol) and excessive EDC (0.06, 0.15, 0.3, 0.6, 0.9, 1.2, 1.5 mmol) were dissolved in 50 mL of phosphate buffer saline (PBS) solution at pH of 5.5 using 1 N HCl solution to activate carboxyl. Then, PEI (0.25 mmol) was added into the mixture solution and then stirred for 4 h at pH of 5.5. Afterward, the unreacted chemicals were removed by dialysis (MWCO: 2000). Finally, Cate-PEI power was obtained after two days of freeze drying. The different molar ratio of caffeic acid to PEI was conducted during the above process. The degree of coupling of catechol on the side chain of PEI was measured using an ultraviolet-visible spectrophotometer at a absorption wavelength of 280 nm. The chemical structure of Cate-PEI was further analyzed by Nuclear magnetic resonance (NMR) spectroscopy.

2.3 Fabrication and characterization of PPH

The PPH was fabricated *in situ* by ferric ion-mediated coordination reaction and oxidative polymerization. Briefly, 4 mg of Cate-PEI aqueous solution (500 μL) with different grafting rates and 35 μL of pyrrole were added into a centrifuge tube to form an evenly mixed solution. Then, 500 μL of iron chloride hexahydrate ($FeCl_3 \cdot 6H_2O$) aqueous solution (0.1 g mL^{-1}) were added into the mixed solution and then let stand. The gelation time was measured by the oblique method and hydrogel performance was determined by the inversion method. In order to observe the microstructure of PPH, Scanning Electron Microscope (SEM) was carried out. In brief, the formed hydrogel was placed in a refrigerator at -80 °C and then freeze-dried for 2 days. Afterward, the frozen hydrogel was cut into half with a knife and the structure of its cross section was observed by Scanning Electron Microscopy (SEM) (JSM-7800F, Japan).

2.4 Instruments and equipment

The dry solid hydrogel was obtained from Freeze dryer (Boyi-kang, Beijing). The composition of the Cate-PEI was analyzed by UV-Vis spectrophotometer (Aoyi, Shanghai). The chemical structure of Cate-PEI was determined by Nuclear Magnetic Resonance (^1H NMR) spectrometer (AVANCE II 400 MHz, Swiss). The cross-section structure of hydrogel PPH was observed by SEM. Rheological properties of PPH hydrogels were characterized by a Thermo HAAKE MARS 60 (HAAKE, Germany). The potential photothermal effects of PPH were investigated by 808 nm NIR optical laser (Leizhiwei, Beijing). The infrared thermal images were recorded by an infrared camera (NO:HT-19) purchased from Dongguan Xintai Instrument & Meter Co., Ltd (Guangdong, china).

2.5 *In vitro* photothermal performance of PPH

In order to evaluate the photothermal performance, 0.1 g of PPH was irradiated by the 808 nm laser for 5 minutes under different power density (0.2, 0.3, 0.5, 0.6 W cm^{-2}) and the temperature was recorded every 20 s. Distilled water was set as a control, the corresponding infrared thermal images were photographed using an infrared camera. To simulate photothermal performance *in vivo*, 0.1 g of PPH in different volume of distilled water (0.1, 0.5, 0.9, 1.3, 1.5 mL) was placed in a EP tube and irradiated by the 808 nm laser (0.6 W cm^{-2}, 5 min). To evaluate the photothermal stability, 0.1 g of PPH hydrogel was subjected into 5 cycles of laser irradiation at 0.6 W cm^{-2} (laser on/off: 5 min), and the temperature was recorded every 20 s.

2.6 Photothermal conversion efficiency of PPH

0.1 g of PPH or 0.1 g distilled water was irradiated by the 808 nm laser at a power density of 0.6 W cm^{-2} for 10 min until a stable maximum temperature, and then the irradiated laser or water was allowed to cool down to room temperature for 10 min. The following formula was used to calculate the photothermal conversion efficiency (η),

$$\sum m C_p \frac{dT}{dt} = Q_{gel} + Q_{Dis} - Q_{Surr} \tag{1}$$

According to the law of conservation of energy, Q_{gel} is the energy input of PPH. Q_{Dis} represents the heat dissipated from the photoabsorption of the sample cell itself. Q_{Surr} is the lost heat energy to the surroundings.

$$Q_{gel} = I(1 - 10^{-A\lambda})\eta \tag{2}$$

$$Q_{Surr} = hS\Delta T \tag{3}$$

where I is the incident power of the NIR laser, and A is the absorbance of PPH at λ of 808 nm. And η is the photothermal conversion efficiency of PPH which means the ratio of absorbed light energy converting to thermal energy, h is defined as the heat transfer coefficient, S refers to the surface area of the measured sample, and ΔT refers to the changes of temperature. In the situation of heating pure water, the heat input is equal to

the heat output at the maximum steady-state temperature, so the equation can be

$$Q_{\text{Dis}} = Q_{\text{Surr}} = hS\Delta T_{\text{Max,water}} \qquad (4)$$

In the whole system, the heat inputs are the heat generated by PPH hydrogel (Q_{gel}) and the heat generated by water (Q_{Dis}), which are equal to the heat output at the maximum steady-state temperature, so the equation can be

$$Q_{\text{gel}} + Q_{\text{Dis}} = Q_{\text{Surr}} = hS\Delta T_{\text{Max,mix}} \qquad (5)$$

According to the eqn (2), (4) and (5), the photothermal conversion efficiency (η) can be expressed as following:

$$\eta = \frac{hS\Delta T_{\text{Max,mix}} - hS\Delta T_{\text{Max,water}}}{I\left(1 - 10^{-A\lambda}\right)} = \frac{hS(\Delta T_{\text{Max,mix}} - \Delta T_{\text{Max,water}})}{I\left(1 - 10^{-A\lambda}\right)} \qquad (6)$$

$\Delta T_{\text{Max,mix}}$ is the temperature change of PPH hydrogel at the maximum steady state temperature, and $\Delta T_{\text{Max,water}}$ is the temperature change of distilled water at the maximum steady state temperature, Only the hS remains unknown for the calculation of (η).

$$hS = \frac{mC_{\text{p}}}{\tau_{\text{s}}} \qquad (7)$$

where m and C_{p} are the mass and heat capacity of solvent (water), respectively. τ_{s} is the system time constant of PPH hydrogel.

$$\theta = \frac{T - T_{\text{Surr}}}{T_{\text{Max}} - T_{\text{Surr}}} \qquad (8)$$

θ is the dimensionless driving force temperature. T_{surr} is the ambient temperature. T is the changing temperature of system surface.

2.7 *In vitro* cytotoxicity

Hydrogel and cells were co-cultured in transwell to investigate the cytotoxicity. Normal fibroblasts (MEF) were planted in the lower culture plate, hydrogels of different quality (25, 50, 100, 200, 400 mg) were placed in the upper chamber, and then incubated with the cells for 24 hours, standard cck-8 kit was used to detect cell viability.

2.8 *In vitro* and *in vivo* MR imaging of PPH

MR imaging of the synthesized PPH was obtained by Nuclear Magnetic Resonance scanner (Germany SIEMENS, Model: Magnetom Trio Tim) to investigate the possibility as a T_2 MR contrast agent. Different amounts of PPH (0.8 mg, 1.6 mg, 2.4 mg, 3.2 mg, 4.0 mg) was placed in a 96-well plate respectively. The measurement parameters were as follows: TR = 3500 ms, TE = 89 ms.

For *in vivo* MR imaging, PPH (100 μL) was injected subcutaneously into the tumor of breast tumor mouse after anesthetize mice with 1% sodium pentobarbital. The retention of PPH were observed *in vivo* at different durations (0 h, 2 h, 24 h, 48 h, 7 d), and the mice pre and post injection were scanned to observe the distribution and retention of the PPH in tumors.

2.9 *In vivo* PTT therapy

All animal procedures were performed in accordance with the Guidelines for Care and Use of Laboratory Animals of Jiangsu University, the animal experiments were conducted according on the Animal Management Rules of the Ministry of Health of the People's Republic of China and approved by the Animal Ethics Committee of Jiangsu University. In order to establish the breast cancer mouse model, female BALB/C mice aged 6–8 weeks were all purchased from experimental Animal Center of Jiangsu University (Permit No. SYXK Su 2018-0053). 4T1 ortho-topic tumor model was established by subcutaneously injecting 100 μL of 4T1 cells (1×10^6 mL^{-1}) into the left breast pad of mice. After establishing a mouse model of breast cancer, anti-tumor photothermal therapy and imaging experiments were conducted.

When the tumor volume reached about 200 mm^3, the mice were randomly divided into three groups (five mice in each group) to receive PPH hydrogel injection *in situ* (100 μL per mouse) including (1) PPH, (2) laser (1 W cm^{-2}, 5 min), (3) PPH + laser (1 W cm^{-2}, 5 min). The temperature changes of the tumor site were measured after 808 nm laser irradiation, and the corresponding thermal images were obtained by the infrared digital camera. The tumor growth and body weight were recorded every 2 days. The tumor volume was calculated according to the following equation: $V = L \times W^2/2$. V represented the tumor volume, L represented tumor length, W represented tumor width.

2.10 *In vivo* biocompatibility of PPH

The potential toxicity of PPH hydrogel was systematically studied *in vivo*. Fifteen healthy female Balb/c mice (6–8 weeks old) were randomly divided into 3 groups: (1) PPH, (2) laser (1 W cm^{-2}, 5 min), (3) PPH + laser (1 W cm^{-2}, 5 min). Twenty days after the injection, liver, spleen, kidney, heart, lung and other major organs and tumors were sliced and stained with hematoxylin and eosin.

2.11 Statistical analysis

All the experimental data were expressed by the mean ± standard deviation (SD). The statistically difference analysis was investigated by one-way of ANOVA using SPSS software. In all the statistical evaluations, $P < 0.05$ was considered significant difference, $P < 0.01$ was considered highly significant difference, and $P < 0.001$ was considered very highly significant difference.

3 Results and discussion

3.1 Preparation and characterization of PPH hydrogel

Inspired by catechol-mediated mussel adhesion, we proposed a novel promising strategy for preparation of multifunctional hydrogel. In order to synthesize PPH, Cate-PEI was firstly synthesized through grafting catechol group to the side chain of PEI *via* the amide reaction. Then, PPH was rapidly formed by

ferric ion mediated coordination reaction and oxidative polymerization (Scheme 1a). Specifically, ferric ion not only served as oxidant to catalyze pyrrole (py) to polypyrrole (PPY), but also as a cross-linking agent to coordinate with the catechol groups on the side chain of the Cate-PEI (Scheme 1b). In addition, the interaction between the resultant PPY and catechol groups further enhanced gelation formation. In order to form the hydrogel at tumor site *in situ*, a double-tube injection device was adopted to control gelation behavior, which was conducive to the adequate coverage completion of photothermal ablation at the tumor area under laser irradiation. Besides, the PPH can be used as a MR contrast agent for real time imaging-guided treatment (Scheme 1c).

We suppose that the grafting degree of catechol on the PEI branch directly affects the formation of hydrogels. Therefore, it is important to regulate and optimize the grafting rate of catechol groups on the side chain of PEI. We choose Nuclear Magnetic Resonance spectroscopy (NMR) and UV-Vis absorption spectrum to investigate catechol grafting and measure the grafting rate. NMR results shown that the presence of the three protons peaks at about 6.5 ppm were clearly visible in the spectrum, which were corresponding with the characteristic peaks of the pure product of catechol, while the individual PEI has no peak. This data preliminarily demonstrated that catechol have been successfully grafted on PEI (Fig. 1a). Then, UV-Vis absorption spectrum further confirmed this result according to characteristic absorption peak at about 280 nm due to benzene ring (Fig. 1b).

Next, a series of Cate-PEI with distinct grafting rate were prepared using DHPPA as catechol precursor. As Table 2 shown, the grafting rate increased gradually as the amount of DHPPA increased and the highest grafting rate reached 39.5%. The reaction products formed by Cate-PEI with different grafting rate (from 0.65%, 2.38%, 7.9%, 17.8%, 33.5%, 36.3%, 39.5%) were noted as PPH-1, PPH-2, PPH-3, PPH-4, PPH-5, PPH-6, PPH-7. The gelation time of different hydrogels was studied by vial-
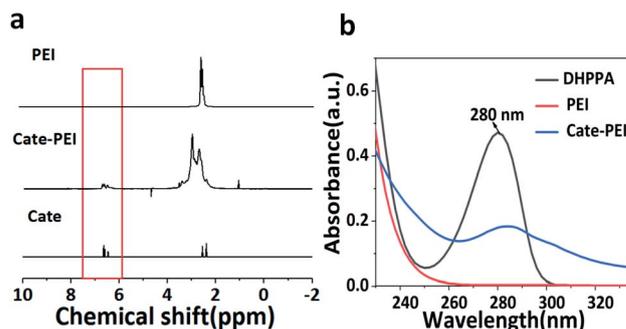

Fig. 1 Optimization of the grafting rate of Cate-PEI. (a) ^{1}H NMR spectra of PEI, Cate-PEI, Cate. (b) UV-Vis absorption spectrum of Cate-PEI.

Table 1 Photothermal conversion efficiency of PPH

$\sum m$	C_p	τ_s	$\Delta T_{Max,mix}$	$\Delta T_{Max,water}$	I (W)	$1 - 10^{-A\lambda}$	η
0.1	4.2	160.76	59.1 °C	3 °C	0.3	0.99	49.3%

tilting method. Fig. 2a shown that PPH-1, PPH-2, PPH-3 could not form hydrogel at any time. Along with grafting rate increasing, PPH-4, PPH-5, PPH-6, PPH-7 exhibited solid rigidity, revealing the formation of hydrogel. The gelation time of PPH-7 with the maximum grafting rate was 10 seconds in Fig. 2b. Therefore, PPH-7 was chosen in subsequent experiments. Next, we investigated gelation performance under each ingredient (Fig. 2c). The results indicated that Cate-PEI and pyrrole, pyrrole and FeCl$_3$, Cate-PEI and FeCl$_3$ did not form hydrogel. In contrast, hydrogel was only formed under Cate-PEI, pyrrole and FeCl$_3$ blending in aqueous solution. It was well known that ferric ion could easily coordinated with catechol group to form
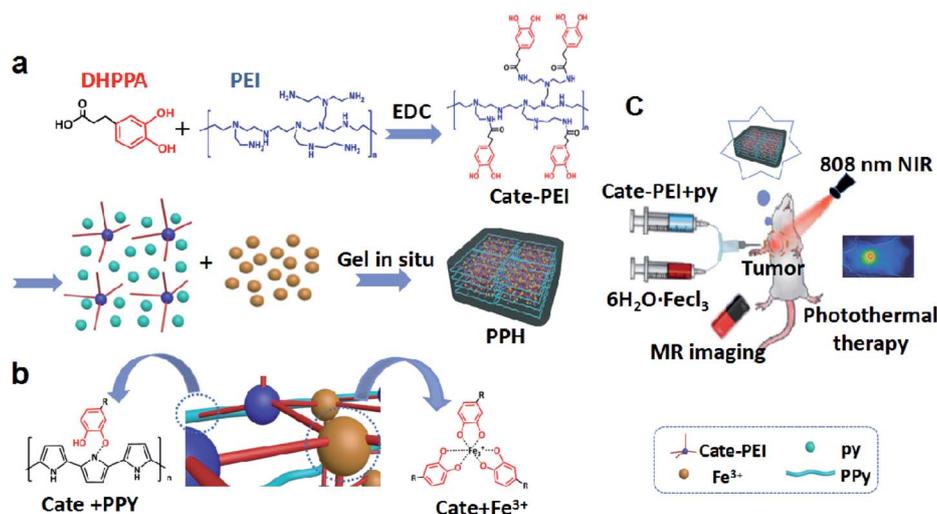
Scheme 1 Schematic illustration of the fabrication of synthetic PPH (a). Potential molecular mechanism model of gelation (b) and its applications *in vivo* (c).

Table 2 The grafting rate under different mole ratio of PEI, DHPPA, EDC

Proportion	1 : 0.2 : 0.24	1 : 0.5 : 0.6	1 : 1 : 1.2	1 : 2 : .4	1 : 3 : 3.6	1 : 4 : 4.8	1 : 5 : 6
PEI (25 000)	0.237 g (0.25 mmol)	0.237 g (0.25 mmol)	0.237 g (0.25 mmol)	0.237 g (0.25 mmol)	0.237 g (0.25 mmol)	0.237 g (0.25 mmol)	0.237 g (0.25 mmol)
DHPPA	0.05 mmol	0.125 mmol	0.25 mmol	0.5 mmol	0.75 mmol	1 mmol	1.25 mmol
EDC	0.06 mmol	0.15 mmol	0.3 mmol	0.6 mmol	0.9 mmol	1.2 mmol	1.5 mmol
Rate (%)	0.65%	2.38%	7.9%	17.8%	33.5%	36.3%	39.5%

stable complex. In spite of this, ferric ion was thought to react with Cate-PEI, but the resultant complex was incapable of forming hydrogel. In view of the finding, we proposed that PPY was likely to play a critical role in metal–catechol hydrogel formation.

After freeze-drying, the cross-sectional morphology of PPH was obtained by scanning electron microscope (SEM) analysis. PPH exhibited a three-dimensional microporous foam network similar to traditional hydrogels[27] (Fig. 2c and d). A lot of spherical particles could be clearly observed in the microporous structure. This might be attributed to the formation of PPY nanoparticles *in situ*.

In order to study the rheological and mechanical properties of PPH, we monitored the storage (G') and loss modulus (G'') and complex viscosity (η^*) of the hydrogel under different strains (0.1–1000%) and different angular frequencies. As shown in Fig. 2e, in the linear viscoelastic region (LVR 0.1–6.524%), the storage modulus (G') was significantly higher than the loss modulus (G''). When the deformation was greater than 6.524%, the storage modulus (G') and loss modulus (G'') both decreased, and hydrogel network structure was destroyed. In the linear viscoelastic region, as the test results of the sample

modulus changing with angular frequency (Fig. 2f), it can be seen that the storage modulus (G') of the sample was slightly higher than the loss modulus (G'') in the entire frequency sweep range. This all confirmed the hydrogel was stable and appeared as a viscoelastic solid. The complex viscosity (η^*) decreased with the increase of angular frequency. This change in mechanical behavior could be attributed to the change in crosslink density in the PPH hydrogels.

3.2 *In vitro* photothermal performance of PPH

PPY has been widely used as an effective photothermal agent in tumor ablation due to its broad near infrared absorption properties. Encouraged by this property, the photothermal performance of PPH was evaluated under 808 nm laser irradiation with different output power. As shown in Fig. 3a, the PPH was exposed to 808 nm NIR irradiation for 5 minutes at different power density (0.2, 0.3, 0.5, 0.6 W cm^{-2}). The temperature of the PPH rapidly heated above 55 °C under irradiation at a low power density of 0.5 W cm^{-2}, but the temperature of pure water did not change significantly. The corresponding thermal images confirmed the conclusion in Fig. 3b. The result shown that the PPH as an ideal photothermal agent had a great potential in
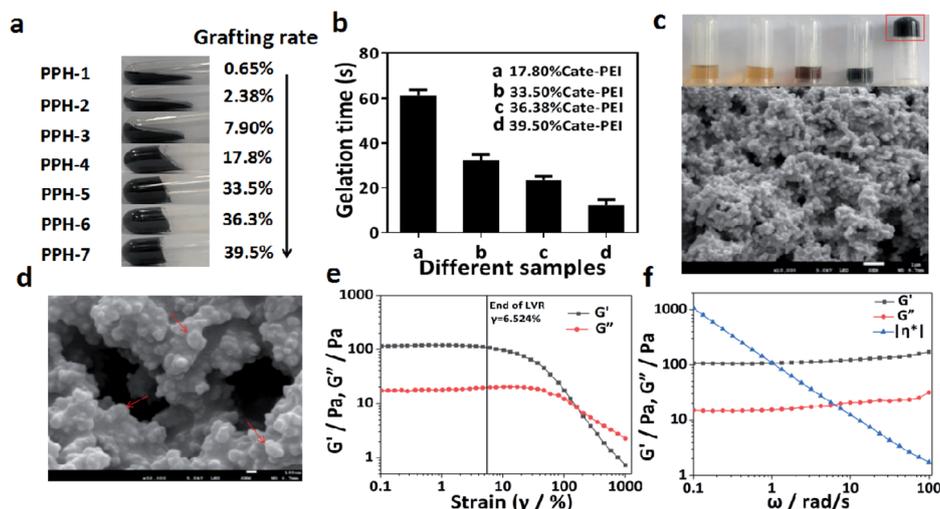

Fig. 2 The analysis of formation and physical characterization of PPH hydrogels. (a) Photographs of PPH-1, PPH-2, PPH-3, PPH-4, PPH-5, PPH-6, PPH-7 after vial-tilting process. (b) The gelation time of PPH-4, PPH-5, PPH-6, PPH-7. (c) Photographs of distinct aqueous solution of combinations and SEM image of the PPH Hydrogel. Tube 1, Cate-PEI; tube 2, Cate-PEI and FeCl$_3$; tube 3, Cate-PEI and pyrrole; tube 4, pyrrole and FeCl$_3$; tube 5, Cate-PEI, pyrrole and FeCl$_3$ (scale bar: 1 μm). (d) Higher-magnification SEM image of the PPH hydrogel. The red arrow pointed to the PPY nanoparticles (scale bar: 100 nm). (e) Storage (G') and loss modulus (G'') at different strain (0.1–1000%) of different hydrogel networks. (f) Storage (G') and loss modulus (G'') and the complex viscosity (η^*) at different angular frequency of different hydrogel networks.
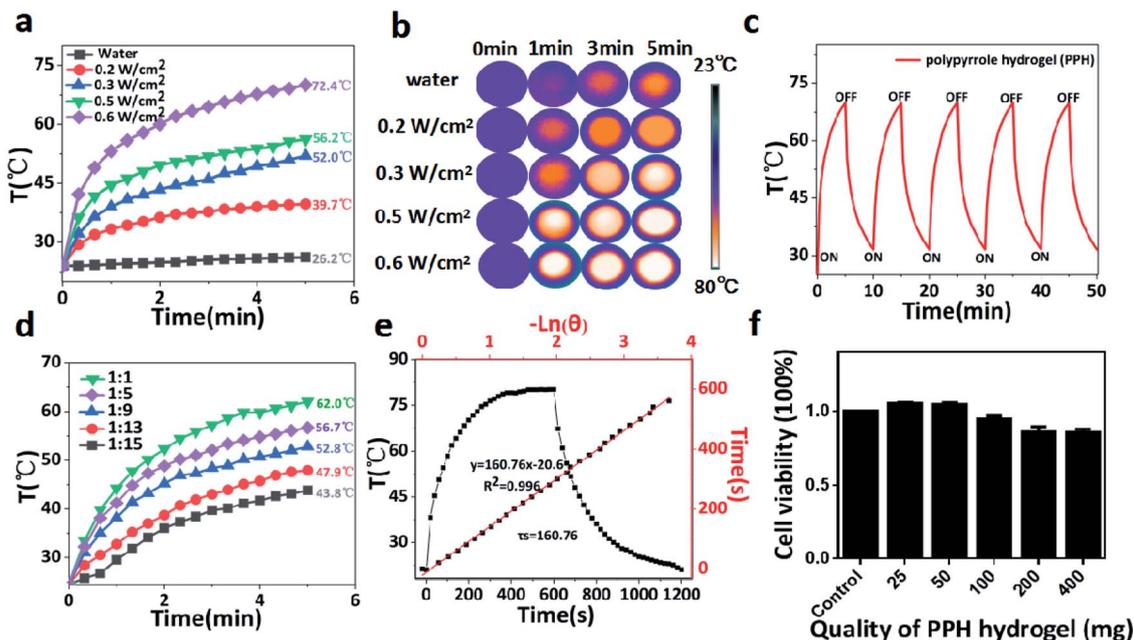
Fig. 3   Characterization of photothermal properties and photothermal conversion efficiency of PPH. (a) Temperature variation curves of PPH under 808 nm laser irradiation at different power density (0.2, 0.3, 0.5, 0.6 W cm^{-2}) for 5 min and (b) corresponding digital images of aqueous solution. (c) Periodic temperature variation curve of PPH during five on/off irradiation cycles laser (in each cycle, laser on time: 5 min, laser off time: 5 min). (d) Temperature variation curves of PPH in different proportions of distilled water ranging from 1 : 1, 1 : 5, 1 : 9, 1 : 13, to 1 : 15 (g : mL) after irradiation at 0.6 W cm^{-2} for 5 min. (e) Calculation of the photothermal-conversion efficiency at 808 nm. Black line: photothermal profile of PPH (0.1 g) irradiated with NIR laser (808 nm, 0.6 W cm^{-2}) to reach a plateau and natural cooling to ambient temperature. Red line: time constant (τ_s) for the heat transfer from the system determined by applying the linear time data from the cooling period. (f) Cell viability of MEF cells after cocultivation with different quality of hydrogels (25, 50, 100, 200, 400 mg) for 24 h.

tumor ablation. In addition, the photothermal effect of PPH was relatively stable without discernible recession after five rounds of repeated laser irradiation (Fig. 3c). Then, the capability of PPH to influence the surrounding environment was further investigated to simulate the photothermal effect in tumor region after *in situ* injection. Briefly, 0.1 g of PPH in different proportions of distilled water was irradiated using NIR laser (808 nm, 0.6 W cm^{-2}) for 5 min in Fig. 4d. The results indicated

that PPH in each group after irradiation could lead to rapid rising of the solution temperature, even when the ratio was up to 1 : 15 (g : mL). According to the reported method, as Table 1 shown, the photothermal conversion efficiency (η)[38,39] of PPH was calculated to be around 49.3% in Fig. 4e and f, which was better than traditional photothermal preparations, including Au nanorods (21%),[40] Cu$_9$S$_5$ nanocrystals (25.7%),[41] WS$_2$ nanosheets (32.8%).[42]
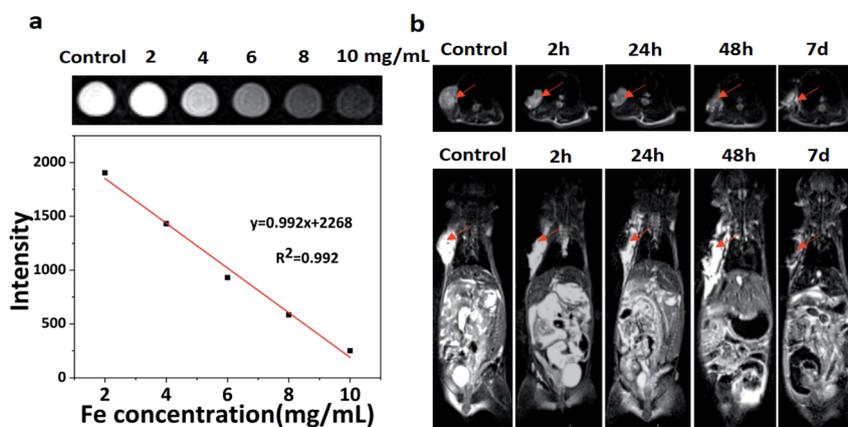

Fig. 4   *In vivo* and *in vitro* MR imaging experiments. (a) T_2-Weighted MR images of PPH at various Fe concentrations (2, 4, 6, 8, 10 mg mL^{-1}). (b) T_2-Weighted MR images of the BALB/C mice bearing 4T1 tumor injected with PPH at different times (0 h, 2 h, 24 h, 48 h, 7 d). The red arrow pointed to the tumor site.
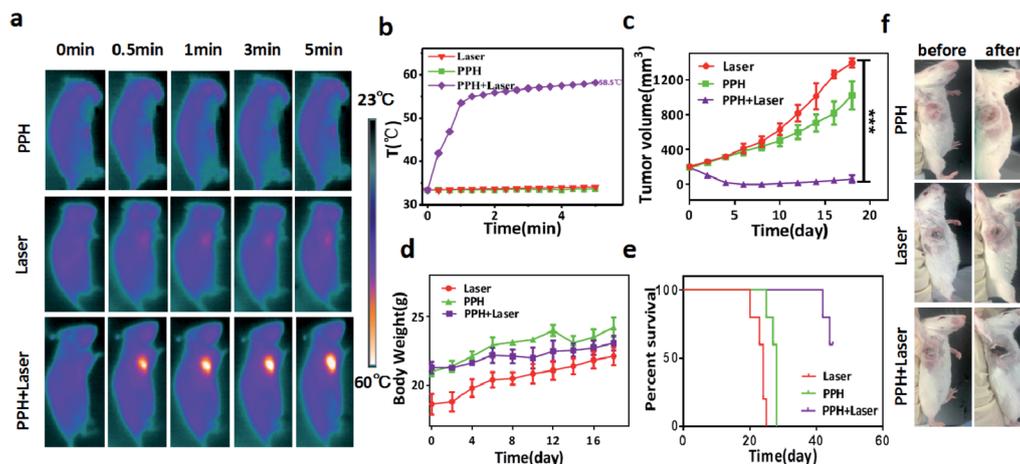
Fig. 5 *In vivo* PTT for treatment of cancer. (a) Infrared thermal images and (b) temperature curve of orthotopic 4T1 tumor *in vivo* under laser irradiation after injection of PPH (100 μL) *in situ*. (c) Tumor growth curves, (d) body weight curves, and (e) survival curves after different treatments ($n = 5$). (f) Mice images of different treatment groups before and 7 days after laser treatment.

3.3 *In vitro* cytotoxicity

The cytocompatibility of PPH hydrogels must be evaluated before *in vivo* experiments in mice. In this study, cck-8 method was used to detect cell viability. PPH hydrogel was co-incubated with MEF cells for 24 h, and cell viability was measured. As can be seen in Fig. 3f, cell viability in distinct treatment was relatively stable. Even at the highest dose of 400 mg of PPH hydrogel, the cell viability still reached 95%. These results indicated that PPH has good biocompatibility and can be applied to biomedicine.

3.4 *In vitro* and *in vivo* MR imaging of PPH

On account of the iron element doped in the PPH during gelation process, we speculated that PPH might be used as contrast agent in MRI for imaging-guided tumor ablation *in vivo*. PBS solution was used as a control for T_2-weighted MR imaging. As shown in Fig. 4a, it can be obviously seen that the signal intensity gradually decreased with the increase of iron

concentration and exhibited good concentration dependent manner. Next, we investigated whether PPH could be used as a T_2-weighted contrast agent for MR imaging in breast cancer mice (Fig. 4b). PPH was injected *in situ* into the tumor region when the tumor volume reached 200 mm^3. A black area in tumor region could be observed after PPH injection at 2 h. After 7 days, the black signal derived from PPH still remained in the tumor site, which demonstrated the excellent imaging capability of PPH *in vivo*. More importantly, these results indicated that PPH was conducive to persistent photothermal therapy without multiple injection. In addition, PPH could be degraded and absorbed under physical condition. Overall, PPH with excellent MR imaging performance could be used to monitor the progress of tumor treatment in real time.

3.5 *In vivo* PTT efficacy of PPH

The therapeutic efficacy of PPH *in vivo* was evaluated in mice bearing orthotopic 4T1 tumor. When the tumor volume reached
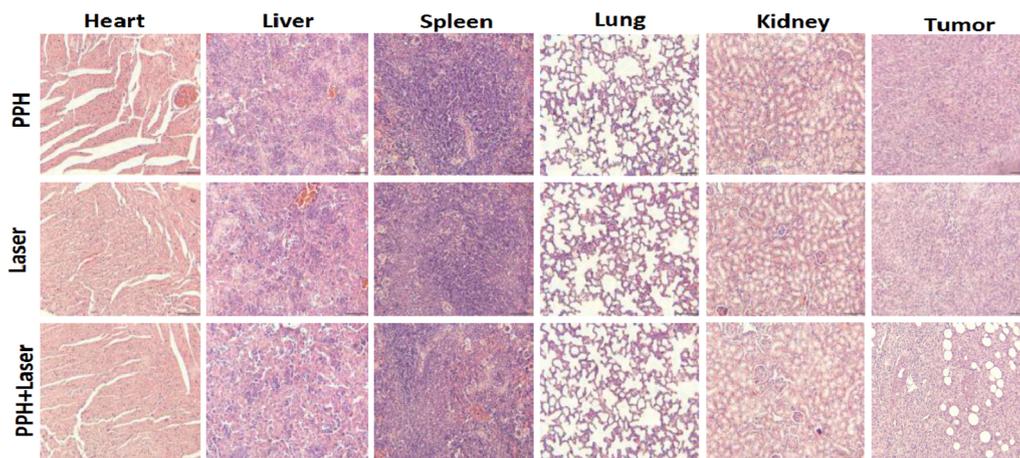

Fig. 6 Representative micrographs of H&E stained slices after the corresponding treatment: (1) PPH; (2) laser; (3) PPH + laser. All images share the same scale bar: (200 μm) ($n = 5$).

200 mm^3, 100 μL of PPH was *in situ* injected into the tumor and irradiated with NIR laser (808 nm, 1 W cm^{-2}) for 5 min. The mice weight and tumor volume was measured during the following 20 days. The temperature change of the tumor was monitored and recorded by an infrared camera under the laser irradiation. In the Fig. 5a and b, it can be seen that the temperature in PPH group or laser groups hardly changed after 5 minutes, but the temperature in PPH combined laser group increased sharply up to 58.5 °C. Furthermore, the mice in PPH combined laser group showed almost complete tumor ablation in 20 days, while mice in PPH group or laser groups showed rapid tumor growth (Fig. 5c). Similarly, we can see from the mice images in Fig. 5f that tumor growth was significantly inhibited after 7 days of combined laser treatment. In addition, the mice in the three groups showed similar trends in body weight. Finally, the average life span of mice in PPH combined laser treatment could be prolonged to 45 days, but that of mice in PPH or laser group was less than 30 days (Fig. 5e). In general, these results indicated that PPH could be served as ideal PTT agent for cancer treatment. As shown in Fig. 6, there were no obvious histological abnormalities or lesions in PPH combined laser group, and the toxicity of the hydrogel *in vivo* is not obvious. After PPH pulse laser treatment, the tumor sections showed obvious vacuolar degeneration, indicating the presence of pathological changes associated with necrosis occurred.

4   Conclusions

To sum up, we have successfully proposed a new method of injectable photothermal therapeutic PPH for MR imaging-guided tumor ablation. Inspired by mussel adhesion, catechol grafted PEI (Cate-PEI) was produced *via* EDC chemical reaction. Then, the PPH was *in situ* synthesized based on ferric ion-mediated simultaneous oxidative polymerization and metal–catechol coordination. The results demonstrated that PPH was capable of fast gelation *in situ* and highly photothermal conversion efficiency up to 49.3%. In addition, PPH could be used as an ideal T_2-weighted contrast agent for MR imaging *in vivo*. Furthermore, PPH could be injected *in situ* into orthotopic tumor, then effectively killed tumor cells and inhibited tumor growth under NIR laser irradiation. This study provides not only a versatile photothermal therapeutic agent for tumor treatment, but also a novel strategy to design and prepare multifunctional hydrogel based on biomimetics.

Conflicts of interest

All authors claim that there is no conflicts of interest.

Acknowledgements

Notes and references

1 G. Ou, Z. Li, D. Li, L. Chen, Z. Liu and H. Wu, *Nano Res.*, 2016, **9**, 1236–1243.

2 Y. Xu, S. Li, Y. Yang, F. Zhou, N. Dong, K. Yan, B. Wang, Y. Zeng, N. Du, X. Li and W. R. Chen, *Theor. Biol. Med. Modell.*, 2019, **16**, 1–11.

3 Y. Guan, *Hepatoma Res.*, 2015, **1**, 159–164.

4 A. S. Schwartz-Duval, C. J. Konopka, P. Moitra, E. A. Daza, I. Srivastava, E. V. Johnson, T. L. Kampert, S. Fayn, A. Haran, L. W. Dobrucki and D. Pan, *Nat. Commun.*, 2020, **11**, 4530.

5 K. Kumar, P. Moitra, M. Bashir, P. Kondaiah and S. Bhattacharya, *Nanoscale*, 2020, **12**, 1067–1074.

6 Z. Zhou, Y. Yan, L. Wang, Q. Zhang and Y. Cheng, *Biomaterials*, 2019, **203**, 63–72.

7 Z. Zhou, Y. Yan, K. Hu, Y. Zou, Y. Li, R. Ma, Q. Zhang and Y. Cheng, *Biomaterials*, 2017, **141**, 116–124.

8 L. Cheng, C. Wang, L. Feng, K. Yang and Z. Liu, *Chem. Rev.*, 2014, **114**, 10869–10939.

9 X. Song, Q. Chen and Z. Liu, *Nano Res.*, 2015, **8**, 340–354.

10 Z. Zha, Z. Deng, Y. Li, C. Li, J. Wang, S. Wang, E. Qu and Z. Dai, *Nanoscale*, 2013, **5**, 4462–4467.

11 Y. Jin, Y. Li, X. Ma, Z. Zha, L. Shi, J. Tian and Z. Dai, *Biomaterials*, 2014, **35**, 5795–5804.

12 J. Li, B. Arnal, C. W. Wei, J. Shang, T. M. Nguyen, M. O'Donnell and X. Gao, *ACS Nano*, 2015, **9**, 1964–1976.

13 X. Chen, M. Zhang, S. Li, L. Li, L. Zhang, T. Wang, M. Yu, Z. Mou and C. Wang, *J. Mater. Chem. B*, 2017, **5**, 1772–1778.

14 Q. Wang, J. Wang, G. Lv, F. Wang, X. Zhou, J. Hu and Q. Wang, *J. Mater. Sci.*, 2014, **49**, 3484–3490.

15 Y. Yang, X. Tai, K. Shi, S. Ruan, Y. Qiu, Z. Zhang, B. Xiang and Q. He, *Theranostics*, 2016, **6**, 2141–2160.

16 P. Gierlich, A. I. Mata, C. Donohoe, R. M. M. Brito, M. O. Senge and L. C. Gomes-da-Silva, *Molecules*, 2020, **25**, 5317.

17 Y. Chao, L. Xu, C. Liang, L. Feng, J. Xu, Z. Dong, L. Tian, X. Yi, K. Yang and Z. Liu, *Nat. Biomed. Eng.*, 2018, **2**, 611–621.

18 Y. Li, J. Rodrigues and H. Tomas, *Chem. Soc. Rev.*, 2012, **41**, 2193–2221.

19 Y. Li, D. Maciel, J. Rodrigues, X. Shi and H. Tomas, *Chem. Rev.*, 2015, **115**, 8564–8608.

20 Y. Li, D. Maciel, H. Tomas, J. Rodrigues, H. Ma and X. Shi, *Soft Matter*, 2011, **7**, 6231–6238.

21 C. Wang, J. Wang, X. Zhang, S. Yu, D. Wen, Q. Hu, Y. Ye, H. Bomba, X. Hu, Z. Liu, G. Dotti and Z. Gu, *Sci. Transl. Med.*, 2018, **10**, 3682.

22 J. Zhao, C. Zhou, C. Wu, H. Wu, C. Zhu, C. Ye, S. Wang and D. Zou, *ACS Appl. Mater. Interfaces*, 2018, **10**, 41947–41955.

23 L. Zhang, J. Zhou, L. Hu, X. Han, X. Zou, Q. Chen, Y. Chen, Z. Liu and C. Wang, *Adv. Funct. Mater.*, 2020, **30**, 1906922.

24 W. Shi, B. Hass, M. A. Kuss, H. Zhang, S. Ryu, D. Zhang, T. Li, Y. Li and B. Duan, *Carbohydr. Polym.*, 2020, **233**, 115803.

25 S. Bhattacharya, R. S. Phatake, S. N. Barnea, N. Zerby, J. Zhu, R. Shikler, N. G. Lemcoff and R. Jelinek, *ACS Nano*, 2019, **13**, 1433–1442.

26 S. Liang, Y. Zhang, H. Wang, Z. Xu, J. Chen, R. Bao, B. Tan, Y. Cui, G. Fan, W. Wang, W. Wang and W. Liu, *Adv. Mater.*, 2018, **30**, 1704235.

27 L. Zhou, L. Fan, X. Yi, Z. Zhou, C. Liu, R. Fu, C. Dai, Z. Wang, X. Chen, P. Yu, D. Chen, G. Tian, Q. Wang and C. Ning, *ACS Nano*, 2018, **12**, 10957–10967.

28 M. Kamra, P. Moitra, D. Ponnalagu, A. A. Karande and S. Bhattacharya, *ACS Appl. Mater. Interfaces*, 2019, **11**, 37442–37460.

29 F. Rizzo and N. S. Kehr, *Adv. Healthcare Mater.*, 2020, **10**, 2001341.

30 A. Andersen, M. Krogsgaard and H. Birkedal, *Biomacromolecules*, 2018, **19**, 1402–1409.

31 H. Lee, N. F. Scherer and P. B. Messersmith, *Proc. Natl. Acad. Sci. U. S. A.*, 2006, **103**, 12999–13003.

32 M. J. Sever, J. T. Weisser, J. Monahan, S. Srinivasan and J. J. Wilker, *Angew. Chem., Int. Ed.*, 2004, **43**, 448–450.

33 J. J. Wilker, *Angew. Chem., Int. Ed.*, 2010, **49**, 8076–8078.

34 Y. He, J. Chen, I. Rafique and Z. Lu, *Eur. Polym. J.*, 2020, **139**, 110025.

35 H. G. Nam, M. G. Nam and P. J. Yoo, *Soft Matter*, 2019, **15**, 785–791.

36 Y. Liu, H. Meng, S. Konst, R. Sarmiento, R. Rajachar and B. P. Lee, *ACS Appl. Mater. Interfaces*, 2014, **6**, 16982–16992.

37 B. R. Lin, C. H. Chen, S. Kunuku, T. Y. Chen, T. Y. Hsiao, H. Niu and C. P. Lee, *Sci. Rep.*, 2018, **8**, 7058.

38 L. Hang, S. Gan, C. Dai, Y. Chen and J. Shi, *J. Am. Chem. Soc.*, 2017, **139**, 16235–16247.

39 W. Ren, Y. Yan, L. Zeng, Z. Shi, A. Gong, P. Schaaf, D. Wang, J. Zhao, B. Zhou, H. Yu, G. Chen, E. M. B. Brown and A. Wu, *Adv. Healthcare Mater.*, 2015, **4**, 1526–1536.

40 C. M. Hessel, V. P. Pattani, M. Rasch, M. G. Panthani, B. Koo, J. W. Tunnell and B. A. Korgel, *Nano Lett.*, 2011, **11**, 2560–2566.

41 Q. Tian, F. Jiang, R. Zou, Q. Liu, Z. Chen, M. Zhu, S. Yang, J. Wang, J. Wang and J. Hu, *ACS Nano*, 2011, **5**, 9761–9771.

42 Y. Yong, L. Zhou, Z. Gu, L. Yan, G. Tian, X. Zheng, X. Liu, X. Zhang, J. Shi, W. Cong, W. Yin and Y. Zhao, *Nanoscale*, 2014, **66**, 10394–11040.